HHS Public Access

Author manuscript

*Acad Radiol*. Author manuscript; available in PMC 2020 March 01.

Published in final edited form as:

*Acad Radiol*. 2019 March ; 26(3): 313–325. doi:10.1016/j.acra.2018.02.028.

# Spatial Heterogeneity of Lung Strain and Aeration and Regional Inflammation during Early Lung Injury Assessed With PET/CT

**Gabriel Motta-Ribeiro**[a], **Tilo Winkler**[a], **Soshi Hashimoto**[a,1], and **Marcos F Vidal Melo**[a]

[a]Dept. of Anesthesia, Critical Care and Pain Medicine, Massachusetts General Hospital, Harvard Medical School, 55 Fruit St, Boston, MA 02114, USA.

[1]Permanent Address: Dept. of Anesthesiology and Intensive Care, Kyoto Prefectural University of Medicine, Kyoto, Japan

## Abstract

**Introduction:** Spatial heterogeneity of lung aeration and strain (change volume/resting volume) occurs at microscopic levels and contributes to lung injury. Yet, it is mostly assessed with histograms or large regions-of-interest. Spatial heterogeneity could also influence regional gene expression. We used positron emission tomography (PET)/computed tomography (CT) to assess the contribution of different length-scales to mechanical heterogeneity and to direct lung injury biological pathway identification.

**Materials and Methods:** Sheep exposed to mild (N=5, supine and N=3, prone) and moderate (N=6, supine) systemic endotoxemia were protectively ventilated. At baseline, 6h and 20h length-scale analysis was applied to aeration in CT (mild groups) and PET transmission (moderate group) scans; and voxel-level strain derived from image registration of end-inspiratory and end-expiratory CTs (mild). 2-deoxy-2-[(18)F]fluoro-d-glucose ($^{18}$F-FDG)-PET kinetics parameters in ventral and dorsal regions were correlated with tissue microarray gene expression (moderate).

**Results:** While aeration and strain heterogeneity were highest at 5–10 mm length-scales, larger length-scales contained a higher fraction of strain than aeration heterogeneity. Contributions of length-scales >5–10 mm to aeration and strain heterogeneity increased as lung injury progressed ($P<0.001$) and were higher in supine than prone animals. Genes expressed with regional correlation to $^{18}$F-FDG-PET kinetics ($|r|=0.81$ [0.78–0.85]) yielded pathways associated with immune system activation and fluid clearance.

**Conclusion:** Normal spatial heterogeneity of aeration and strain suggest larger anatomical and functional determinants of lung strain than aeration heterogeneity. Lung injury and supine position increase the contribution of larger length-scales. $^{18}$F-FDG- PET-based categorization of gene expression results in known and novel biological pathways relevant to lung injury.

**Corresponding Author:** Gabriel Motta-Ribeiro, Department of Anesthesia, Critical Care and Pain Medicine, Massachusetts General Hospital and Harvard Medical School, 55 Fruit St, Boston, MA 02114, USA. Electronic : gabrielcasulari@poli.ufrj.br. gabrielcasulari@poli.ufrj.br, twinkler@mgh.harvard.edu, soshi@koto.kpu-m.ac.jp, VidalMelo.Marcos@mgh.harvard.edu

**Keywords**

Computed Tomography; Positron Emission Tomography; Strain; Gene Expression

## Introduction:

Excessive mechanical forces can produce lung injury during mechanical ventilation. Indeed, regional strain (change in lung volume/resting lung volume) has been shown to relate to local lung inflammation particularly in the presence of systemic inflammation.[1] Excessive mechanical forces can occur not only at large lung areas of hyperinflation[2] but also at the microscopic level. Experiments utilizing total lung capacity (TLC) maneuvers in excised dog lobes revealed heterogeneity of regional gas volume changes in relation to gas volume at TLC at length-scales as small as ~2 mm.[3] In fact, pressure-volume relationships determining lung expansion are related to properties that scale down to the microscopic level of collagen and elastin fibers.[4] A theoretical study indicated that mechanical stress is significantly amplified around collapsed alveoli.[5] Despite the relevance of such small length-scale phenomena, most studies on pulmonary static and dynamic strain are based on whole lung[6,7] or large regions-of-interest (ROI).[1,8] Given that heterogeneity of lung expansion is relevant to lung injury, it is important to understand its topographic basis. Yet, information is scant on the length-scales contributing to strain and aeration heterogeneity during mechanical ventilation. Computed tomography (CT) imaging and elastic registration allow for estimation of a range of such length-scale contribution by assessment of *in vivo* regional tissue strain and aeration.

Lung injury results from complex interactions among mechanical and biological factors.[9] The inflammatory response to local and global stimuli includes recruitment of cells such as neutrophils and affects pulmonary regional metabolic activity, allowing for its *in vivo* assessment with the positron emission tomography (PET) tracer 2-deoxy-2- [(18)F]fluoro-d-glucose ($^{18}$F-FDG).[10–15] Recently, we showed that $^{18}$F-FDG-PET could provide an early imaging biomarker for acute respiratory distress syndrome (ARDS) before this condition is clinically established, as well as guide tissue sampling for gene expression analysis.[10] Of note, $^{18}$F-FDG-PET kinetics allows for estimation of parameters characterizing tissue phosphorylation rate, associated with tumor aggressiveness and response to therapy in oncological studies[13,14] and with cytokine gene expression in experimental acute lung injury (ALI).[12] Accordingly, $^{18}$F-FDG-PET kinetics parameters could be a promising tool to guide the analysis of gene expression datasets and identify pathways relevant to the mechanism and treatment of ALI.

We hypothesized that: 1) in normal lungs, small length-scales contribute significantly to heterogeneity of parenchyma expansion and that these contributions differ for aeration versus strain due to their anatomical and functional determinants; 2) contribution of length-scales to total strain and aeration heterogeneity is affected in the early stages of lung injury and depend on body position (supine versus prone); and 3) the distinct regional processes leading to pulmonary inflammation during early lung injury result in regional parameters of $^{18}$F-FDG-PET kinetics that signalize gene expression patterns consistent with pathways

relevant to lung injury. We explored these hypotheses in sheep models of mild and moderate endotoxemia during the first 20–24h of mechanical ventilation with clinically relevant ventilatory settings.

## Materials and Methods:

Data derived from two independent sets of sheep models of ALI with systemic inflammation (endotoxemia) and mechanical ventilation. Experimental protocols were approved by the Subcommittee on Research Animal Care and in accordance with the "Guide for the Care and Use of Laboratory Animals" (National Institutes of Health publ. no. 86–23, revised 1996).

### Experimental protocol

All animals were anesthetized, paralyzed and ventilated with volume-controlled ventilation and low tidal volume according to the ARDSNet low positive end-expiratory pressure (PEEP) protocol.[16] Initial settings were tidal volume=6 ml/kg (adjusted to reach an alveolar plateau (phase III) at volumetric capnography); PEEP=5 $cmH_2O$; inspired oxygen fraction=0.3 (adjusted to maintain arterial oxygen saturation ≥90%); inspiratory-to-expiratory time ratio=1:2; and respiratory rate aiming at an arterial carbon dioxide partial pressure within 32–45 mmHg. An alveolar recruitment maneuver with application of airway pressure at 40 $cmH_2O$ for 30 s was performed at baseline to expand lung units and standardize lung history. Data were collected at baseline, 6h and end of the experiment (20–24h). After baseline measurements, endotoxin was intravenously infused throughout the experiment to model either moderate (10 ng/kg/min, *Escherichia coli* 055:B5, List Biologic Laboratories Inc, Campbell, CA) or mild (2.5 ng/kg/min) endotoxemic states.

## Moderate endotoxemia

Six sheep were anesthetized with ketamine, propofol and fentanyl, and paralyzed with pancuronium. After 20h of mechanical ventilation and endotoxemia, animals were euthanized and imaging-guided tissue samples harvested for gene expression analysis. Details on anesthetic and ventilatory management, and tissue sample collection and RNA extraction have been previously described.[10]

### Imaging protocol and processing.

The moderate endotoxemia experiment was exclusively based on PET techniques. The PET camera (Scanditronix PC4096; General Electric, USA) collected 15 transverse slices of 6.5 mm yielding a 9.7-cm-long field-of- view (~70% of total lung volume).[17] Images consisted of an interpolated matrix of 128×128×15 voxels (2.0×2.0×6.5 $mm^3$). Scans were acquired in stationary mode as:

*1)* Transmission scans: rotating pin-source ($^{68}Ge$, 10 min) to correct for attenuation in emission scans, calculate the gas fraction ($F_{GAS}$) of ROIS from the measured regional density[18] ($F_{GAS}$=l-regional density), and delineate the lung mask for image analysis. Reconstruction used filtered back projection with a Hanning filter of 11.5 mm width (full width at half maximum, FWHM ~13 mm).[19]

*2)* Emission scans: $^{18}$F-FDG tracer used to assess lung metabolic activity.[20] Tracer dissolved in 8 ml saline (~40 MBq at 0 h and ~200 MBq at 6 and 20h) was infused at a constant rate through a jugular catheter for 60 s. Starting with $^{18}$F-FDG infusion, dynamic PET scan was acquired for 75 min (40 frames: 9×10,4×15,1×30,7×60,15×120,1×300, and 3×600 s). Plasma samples of $^{18}$F-FDG activity in pulmonary arterial blood were measured at 5.5, 9.5, 25, 37, and 42.5 min to calibrate an image-derived input function.[11] Metabolic activity was estimated from the regional $^{18}$F-FDG net uptake rate ($K_i$=Fe $k_3$) using a Sokoloff model, which comprises the fractional distribution volume of $^{18}$F-FDG available for phosphorylation (Fe) and the rate of phosphorylation ($k_3$). Fe (=$K_1$/($k_2$+$k_3$)) increases with the $^{18}$F-FDG that enters tissue from blood at a rate $K_1$ and decreases when $^{18}$F-FDG returns to blood at a rate $k_2$ or is phosphorylated. In addition, this model provided Fb (ROI's blood fraction), used to calculate regional tissue fraction ($F_{TIS}$=1- $F_{GAS}$-Fb). The parameter identification method also estimated the blood transit time ($t_d$) from the heart to studied ROIs.[20] Emission scans were reconstructed with a filter width of 6.4 mm.

### Transcriptome-wide gene expression analysis.

Gene expression in tissue samples from dependent (dorsal) and non-dependent (ventral) regions were quantified using species-specific microarray analysis (Agilent Technologies, USA). We used fluorescence quantification, proportional to the amount of RNA hybridized with 15,208 different single-stranded DNA. Genes already identified among that DNA set were selected from a manufacturer's updated list (July 3, 2017) excluding entries classified as predicted. There were 1,033 unique genes available. Dorsal/ventral ratio of gene expression was correlated to corresponding ratios of $k_3$, $F_{TIS}$ and tissue-specific Ki (Kis=Ki/$F_{TIS}$) and Fe (Fes=Fe/$F_{TIS}$) estimated at 6h. For genes measured more than once in the array, the average expression was used.

### Mild endotoxemia

Eight female sheep were studied for length-scale analysis of aeration and strain. Animals were sedated with intramuscular ketamine and midazolam, and anesthetized with propofol, ketamine and fentanyl. Paralysis was established with rocuronium. After intubation, lungs were mechanically ventilated with low-PEEP ARDSNet principles[16] for 24h in supine (N=5) or prone (N=3) position. Sheep were positioned in the NeuroPET/CT scanner (Photo Diagnostic Systems Inc., USA) using CT scans during controlled breathing to maximize lung volume within the field-of-view. Details on anesthesia and mechanical ventilation are provided in an accompanying paper.

### Imaging protocol.

The mild endotoxemia experiment used PET/CT techniques. CT scans (tube current of 7 mA and voltage of 140 kVp) were acquired during breath holds at end-inspiration (plateau pressure) and end-expiration (PEEP) for strain analysis. Mean lung volume CT images (120–140 kVp) were acquired during tidal breathing (2 min) for aeration analysis. Images comprised a matrix of 512×512×82 voxels (0.49×0.49×2.5 mm$^3$).[21] CT images were converted to $F_{GAS}$ considering tissue density equal to 0 Hounsfield units (HU) and air density equal to −1000 HU, $F_{gas}$=HU/−1000.

### Strain estimation.

Voxel-level strain was assessed using elastic image registration to identify the transformation T(x) that mapped each end-inspiratory image back to the corresponding end-expiratory image. Before registration, images were rescaled to achieve within lung parenchyma a minimum of zero and a maximum of one. Each dimension was cropped to the boundaries of the end-inspiratory mask and padded with a margin of 50 voxels at each side. Registration was implemented with diffeomorphic transforms and B-spline spatial regularization in a multistage approach (increasing image resolution and decreasing B-spline knots' distance), using the open source Advanced Normalization Tools (ANTs).[22] From T(x) the volumetric deformation of each voxel was quantified by the determinant of the Jacobian (directional derivative) matrix.[23–26] This provides the ratio of the final to the initial volume. Strain is then defined as *Jacobian-1* and is referenced to overall volume (tissue+blood+air) at end-expiration.

In the main analysis, the B-spline knots' distance for the first stage was 26 mm and was halved at each one of the three subsequent stages. We tested the influence of that parameter in the contribution of different length-scales to strain heterogeneity (see below, Length-Scale Analysis) by estimating T(x) with initial knots' distances of 13, 52 and 130 mm and the same strategy for distance reduction. Overall accuracy of image registration with each knots' distance was assessed by the standard method of distance between landmarks. In three supine animals (two at baseline and 24h and one at 6h) landmarks were automatically defined in the expiratory image and semi-automatically matched in the inspiratory image.[27] A perfect registration would result in a distance equal zero.

### Image noise estimation.

The level of noise in the mean lung volume CT at full resolution was estimated by two different methods based on histograms of local standard deviations (SD), i.e. estimated in a neighborhood of each voxel, within homogenous ROIs. The first method used the difference between lines and columns to suppress the influence of the image content on the SD.[28] The noise SD was calculated from the parameters of an iterative fitting of the local SD distribution to a chi-square. We implemented it slice-by-slice considering voxels within the lung mask and the following control parameters: histogram limit $k_{max}$=number of voxel/200, expansion factor $\alpha$=0.25 $k_{max}$/mean(voxel's value) and fitting gain $\beta$=2.12. Global SD was the mean of all slices. The second method calculated the local SD in each slice and designated the global SD as the peak of the histogram in voxels classified as soft-tissue (0<HU<100), considered homogenous.[29] We used a neighborhood of 9 mm for the local SD estimation and a histogram of 200 bins.

### Selection of voxels for analysis

Initial lung masks were generated by selecting aerated regions with a fixed threshold. For the moderate endotoxemia experiments, this was combined with perfused regions from $^{13}$NN-PET scans.[30] For the mild endotoxemia experiments, non-aerated regions were manually delineated. All masks were manually refined to exclude large bronchi and pulmonary vessels. Within the lung mask, regional $^{18}$F-FDG kinetics were computed in three adjacent ROIs of equal height.

### Aeration levels

Fgas images were divided into non- ($F_{GAS}$<0.1), poorly- (0.1<$F_{GAS}$ <0.5), normally- <(0.5<$F_{GAS}$<0.85) and hyper-aerated ($F_{GAS}$>0.85) compartments expressed as a fraction of lung mass.[31]

### Length-Scale Analysis

To quantify the size of sources of heterogeneity contributing to the total variability within the lungs, we applied length-scale analysis[30,32] to aeration and strain images. In this technique, images are spatially low-pass filtered using a series of pre-determined filter sizes. For each filter size, image heterogeneity is quantified as the variance of the variable being studied (aeration or strain) normalized by the squared mean, equivalent to the squared coefficient of variation. The contribution of each length-scale range to total heterogeneity is calculated as the difference in the normalized variances among consecutive filter sizes. We used a moving average filter with a cylindrical kernel, height equal to the diameter, and sizes of 13 to 91 mm (13 mm step) for aeration and 5 to 90 mm (5 mm step) for strain (and aeration from CT). Results were expressed relative to the smallest length-scale of each range to eliminate the effects of global heterogeneity changing along the experiment. Linear vertical gradients due to gravity affecting aeration and strain were subtracted from images before filtering.[30,33]

### Statistical Analysis

Data are expressed as mean±SD or median [$25^{th}$-$75^{th}$ percentile]. All tests were two-tailed and performed in R 3.3.1 (R Foundation for Statistical Computing, Vienna, Austria), unless otherwise noted.

Aeration and strain analysis: Aeration compartments were compared between time points and experimental conditions, and length-scales relative contributions (aeration and strain) were compared between ranges and time points, using linear mixed-effects models (animal random intercept). Interactions were included when significant. Multiple comparisons p-values were calculated from multivariate *t* distributions. CT noise was compared between and within methods by repeated measurements ANOVA. Significance was set at $p<0.05$.

Gene expression analysis: we used Pearson correlation coefficient to determine the association between dorsal/ventral ratios of microarray derived gene expression and $^{18}$F-FDG-PET kinetics parameters $k_3$, Fes, and Kis, as well as $F_{TIS}$. Gene sets for each of these parameters were produced by selecting correlations with significance level $p<0.1$. Biological pathways derived from these gene sets were identified using DAVID software[34] (National Institute of Allergy and Infectious Diseases, USA) with default settings: at least two genes and EASE<0.1.

## Results:

Regional aeration differed among the experimental conditions. Supine mildly endotoxemic animals showed the largest fraction of lung mass regions with 0.1<Fgas<0.5 throughout the

experiment (Figure 1A). Regions with Fgas<0.1 increased in both supine groups (Figure 1A). Only supine animals presented a vertical gradient of aeration (Figure 1B).

### Length-Scales of Aeration Heterogeneity

In all cases, aeration heterogeneity at mean lung volume was predominantly present at the 13–26 mm length-scales (Figure 2). The relative contribution of larger length-scales increased as lung injury progressed (Figure 2). Of note, the higher the mean aeration of an animal, the lower was the contribution of larger length-scales (Figure 2D). Mildly endotoxemic supine animals, which presented lowest mean aeration, had the highest contribution of large length-scales, while prone animals had the lowest (Figure 2D).

High resolution CT acquired in the mildly endotoxemic sheep allowed us to analyze length-scales smaller than those obtained with PET transmission scans in moderately endotoxemic sheep, and to calculate voxel-level tidal strains. Increasing the resolution of the length-scale analysis reinforced the predominant contribution of small length-scales to aeration heterogeneity, and the higher contribution of larger length-scales in supine versus prone animals (Figure 3). Importantly, the estimated noise level in the CT images was similar with both estimation procedures, did not change with time and was at least two-fold below the SD of voxels inside the lung mask filtered with the 5-mm kernel (Table 1).

### Length-scales of Tidal Strain Heterogeneity

Tidal strain heterogeneity was predominantly present at length-scales of 5–10 mm (Figure 4). Supine animals presented higher relative contributions of larger length-scales than prone animals (Figure 4). The two body positions differed in their time course. The contribution of length-scales to tidal strain heterogeneity did not change with time in prone animals (Figures 4) despite change in their length-scales contribution to aeration heterogeneity (Figures 2B and 3). In contrast, an increase of the contribution of larger length-scales to strain heterogeneity was observed already at 6h in supine animals, and more evident at 24h (Figure 4).

Before evaluating the effect of varying B-spline knots' distances on the relative contributions of length-scale ranges to strain heterogeneity, we tested the overall accuracy of the different registration results using landmarks. The best agreement was at 0h (Figure 5) and length-scales were compared only at baseline. Of note, for all knots' distances >13 mm, the $75^{th}$ percentile of the combined landmarks distances was below the largest dimension of a voxel (2.5 mm).

The sizes of the features in strain images increased with the knots' distance, as expected (Figure 6A). However, the relative contribution of length-scales was not affected when initial knots' distances of 13 or 52 mm were compared to the 26 mm used in our main analysis (Figure 6B). The initial regularization to 130 mm markedly altered the heterogeneity length-scales, increasing the contributions of all ranges (Figure 6B). With this regularization, after 24h the increase in contribution was significant for length- scales larger than 30 mm (Figure 6C).

### Regional Phosphorylation Rates and Gene-Expression

Regional kinetics of $^{18}$F-FDG in lung regions of distinct aeration (and likely distinct tidal strain) was significantly different for phosphorylation rate ($k_3$) and tissue-specific $^{18}$F-FDG-uptake rate (Kis) at 6h (Figure 7). Therefore, while ventral and dorsal regions had similar metabolic activity at 0 and 24h, changes in that metabolic activity followed different temporal trajectories.

We tested if these different trajectories resulted from differences in regional biological processes correlating the dorsal/ventral ratio of $^{18}$F-FDG kinetics parameters at 6h and the gene expression from species-specific microarray analysis. The Kis was correlated to 35 genes with an absolute correlation coefficient |r|=0.81 [0.78–0.85]. Ontology analysis of these genes revealed two pathways linked to metabolism (Table 2). The tissue-specific $^{18}$F-FDG volume of distribution (Fes) showed 106 correlated genes (|r|=0.81 [0.78–0.85]) with pathways associated to the immune system and environmental sensing (Table 2 and Table A. 1). The $k_3$ was correlated to 30 genes (|r|=0.84 [0.78–0.90]) and a sodium transport pathway. Of note, $k_3$ was correlated to expression of hexokinase and Fes to expression of toll-like receptors TLR2 and TLR4 (Figure 8). Several Kis correlated genes were also correlated with either Fes (n=17) or $k_3$ (n=9). In contrast, there was no gene expressed in simultaneous correlation with Fes and $k_3$. Finally, the regional differences of $F_{TIS}$ were correlated to 59 genes (|r|=0.80 [0.76–0.84]). The identified pathways overlapped with Fes (Table 2 and Table A.1).

## Discussion:

Our main findings are that in the first 20–24h of lung injury due to systemic endotoxemia and mechanical ventilation: 1) spatial heterogeneity of lung strain and aeration are predominantly present at small length-scales (≤5–10mm) in normal and initially injured lungs. Length-scales >5–10 mm contribute more to strain than to aeration heterogeneity suggesting lung regions of size comparable to the secondary pulmonary lobule as the source of strain heterogeneity and regions smaller than that as the source of aeration heterogeneity; 2) acute lung injury and body position importantly affect the relative contribution of length-scales >5–10 mm to strain and aeration heterogeneity, which increase as lung injury progresses and is larger in heterogeneously (supine) than homogeneously (prone) expanded lungs; and 3) a novel approach to analyze gene expression by using *in vivo* PET-measurement of regional $^{18}$F-FDG kinetics reveals pathways consistent with the studied lung injury process, and suggests novel pathways of potential relevance for mechanistical studies and treatment.

### Methodological Considerations

Decomposing the spatial variability of PET and CT images using length-scale analysis allows characterization of the size of features in the images contributing to total heterogeneity (Figure A. 1). In contrast, global histogram methods characterize the variability among voxels without considering the spatial relation among neighbors. Compared to frequency analysis methods, length-scale analysis does not include assumptions about the periodicity of spatial variations, and does not require an infinite

frequency spectrum to represent sharp localized image features. Length-scale analysis is related to methods of fractal analysis such as box counting. However, instead of providing a single number across length-scales (e.g., the global fractal dimension), it provides a set of measures of the contribution of different spatial sizes to total heterogeneity. Importantly, a filter kernel size that is not an integer multiple of the real length-scale generates periodic signals in the frequency domain, resulting in smoother transitions between length-scales (Figure A.1). On the other hand, due to this smooth characteristic, low-pass filtering is less sensitive to grid misalignment compared to the box counting method.[33]

Technical features of the hardware and software utilized for image acquisition and processing affect length-scale analysis. Noise, true resolution, and contrast recovery influence the overall transfer function, which determines how the true variability within the lungs is represented in an image. Accordingly, when analyzing length-scales derived from different imaging systems, factors such as radiation dose, detectors (noise level), modulation transfer function and reconstruction kernel filters must be considered. Image noise affects mostly the small length-scales and would be of particular concern for the 5–10 mm aeration length-scale. Our noise estimation within each image was markedly smaller than the SD for the lung voxels after filtering with a 5-mm kernel. This shows that noise was not the main factor for the length-scale results.

Elastic image registration involves spatial regularization, which smoothes the estimated vector field of tissue displacement between two images to suppress effects of imaging noise on the local estimates. This corresponds to a spatial filter, which in our study was determined by the B-spline knots' distance, and could affect the assessment of relative contributions of the different length-scales to total heterogeneity. We tested initial knots' distances of 13, 26, 52 and 130 mm resulting in 1.625, 3.25, 6.25 and 16.25 mm at the final registration step. If the regularization would affect the relative contribution of length-scales, the contribution of length-scales >5–10 mm should have been lower for the 13 mm knots' distance, and higher for the 52 mm. However, substantial differences were only observed with 130 mm, in which the final knots' distance was between the second and third length-scales. Thus, registration parameters could influence the length-scale analysis, but would not be of sufficient magnitude to affect their biological meaning for smaller knots' distances.

### Length-Scale Analysis of Aeration and Tidal Strain Heterogeneity

We found that the largest contribution to aeration and strain heterogeneities was at the 5–10 mm length-scale. The spatial distribution of aeration and strain depend on anatomical and functional factors. Anatomically that observed length-scale ranges from a human acinus (set of alveoli at a terminal airway)[35] to secondary pulmonary lobules (3 to 12 acini marginated by connective tissue).[36] Functionally, local aeration of normal lungs is determined by local parenchyma elastic and resistive properties, and the effect of neighboring units (interdependence). The mechanical properties of parenchyma depend at least on the elements of the extracellular matrix, the alveolar surface tension and the transpulmonary pressure.[4] For strain, different end-expiratory aerations correspond to distinct states of the tissue stress-strain curve leading to different changes in size of alveolar units for the same change in pressure. In addition, local gas flow depends on the impedance of the path from

the trachea to the first-order bronchioles at the acini. Previous studies indicate the presence of substantial expansion heterogeneity at the microscopic level,[37,38] while images of aeration and ventilation distribution with different modalities suggest homogeneity at larger length-scales.[32,39] Thus, our results are consistent with a predominance of the contribution of small length-scales to total heterogeneity in normal lungs.

The relative contribution of length-scales to aeration and tidal strain heterogeneity reveals important differences in their spatial distributions. Length-scales >10 mm contributed significantly more to strain heterogeneity than to aeration heterogeneity. This suggests that substantial strain heterogeneity occurs at lung regions with sizes comparable to or larger than the secondary pulmonary lobule (~10 mm),[36] while aeration heterogeneity relates predominantly to acinar sizes (~2.5 mm). This finding is consistent with magnetic resonance measurements of the size of airspaces using the apparent diffusion coefficient of $^{3}$He.[40] The greater contribution of larger length-scales to strain heterogeneity may result from a combination of tissue interdependence influencing the expansion of neighboring lung units with the influence of similar gas flow to acini in a secondary pulmonary lobule, supplied by a single small bronchiole.[36] Our findings are also consistent with measurements of fractional lung expansion using parenchymal markers in excised lobes, which indicated that the linear dimension of anatomic units producing expansion variability was ~10 mm.[41] Highly heterogeneous static and dynamic inflation of neighboring small lung units could result in injurious shear stress. Importantly, differences at these length-scales would hardly be seen with previously applied regional strain analysis in large ROIs.[1,8]

While small length-scales contained the largest fraction of aeration heterogeneity, length-scales as large as 78 mm still presented a sizeable contribution to heterogeneity at baseline (normal lungs). The contribution of these larger length-scales was markedly different between prone and supine positions. Supine animals had higher relative contributions to total aeration heterogeneity at all length-scales as compared to prone animals, and a lower decrease in these contributions as length-scales increased. Because we removed the gravitational gradient from the spatial distribution of aeration, the quantified heterogeneity cannot be explained merely by dependent lung atelectasis but implies regional differences present at the same vertical level, with aeration heterogeneities up to anatomical sizes compatible with lobes (~7 cm).

Progress of ALI increased the contribution of larger length-scales not only to aeration, but also to strain heterogeneity. For aeration heterogeneity of supine animals changes from 0 to 6h predominated at length-scales >25–30 mm, and extended to all length scales at 24h. This could be due to increase in aeration variability in regions of poor aeration[32] (dorsal areas), and is consistent with growth of such poorly aerated regions. Strain heterogeneity of supine sheep, on the other hand, was affected at the small length-scale range from 0 to 6h followed by an increase at all length-scales at 24 h. Such findings agree with previous studies showing increased heterogeneity of specific ventilation at small length-scales within poorly aerated areas (1.75 mm using K-edge CT imaging[39] and <12 mm with $^{13}$NN-PET).[32] For the homogenously aerated prone animals, the relative contribution of length-scales to total heterogeneity changed only for aeration at 24h, with no change observed for strain. Thus,

changes in strain length-scale could indicate change in deformations within lung regions before major redistribution of strain between regions of different aeration.

The approximately exponential decrease in the contribution of length-scales to aeration and strain heterogeneity as length-scale increases is consistent with the proposed fractal characteristic of the airway tree.[42] Accordingly, increase in length-scale during mechanical ventilation and endotoxemia could be a marker of lung mechanical conditions conducive to injury. Of note, the change of length-scales contribution at 24h was almost a parallel shift from baseline suggesting that at early stages of ALI, changes in regional mechanical properties would not overcome other anatomical determinants of aeration and strain spatial distributions.

## Gene Expression Analysis

Supine animals presented differences between ventral and dorsal aeration. Given that regional mean aeration is associated with heterogeneity in aeration and specific ventilation, [32] a measurement closely related to strain, we presumed that biological mechanisms would differ between those regions. We previously demonstrated that changes in regional metabolic activation precede changes in regional lung density, clinically used for diagnosis, in the early stages of ARDS.[10] Based on such findings, we now identified pathways derived from genes topographically expressed at magnitudes corresponding to regional metabolic parameters, i.e., correlation between dorsal/ventral ratios of gene expression and $^{18}$F-FDG kinetics parameters. This molecular imaging-guided method to identify gene expression differs from previous methods based on whole lung analysis.[43,44] It aims to advance those by objectively studying lung areas with quantitatively determined distinct metabolic features.

The pathways related to Fes revealed the sensing and response to inflammation with toll-like receptors, TNF[45] and NF-kappa B[46] signaling. Such finding reinforces the validity of the proposed method to identify relevant processes and confirms the expected relevance of those pathways during ALI. Fes quantifies the amount of $^{18}$F-FDG available to phosphorylation (i.e., the $^{18}$F-FDG volume of distribution, Fe) normalized to tissue mass. Correlation of Fes with TLR4 suggests the topographical association of Fes with lipopolysaccharide recognition[47] and recruitment of neutrophils, consistent with the interpretation of Fe as influenced by the regional number of neutrophils.[15] Tissue fraction had similar pathways to Fes, likely due to the spatial distribution of tissue coinciding with higher blood flow (and transport of endotoxin) in dorsal regions,[10] lung injury leading to tissue consolidation[48] or to increased $F_{TIS}$ due to more immune system cells.

The $^{18}$F-FDG phosphorylation rate ($k_3$) was correlated to the pathway of aldosterone-regulated sodium reabsorption. This pathway is linked to the epithelial sodium channel (ENaC) that acts to regulate the sodium balance in a cell. In the lungs, it is linked to fluid transport from the alveolar space. Thus, ENaCs are important for clearance of lung edema.[49] Such findings suggest an increased activity of ENaC in regions with high $k_3$ possibly to overcome increased epithelial permeability. $k_3$ was also positively correlated with expression of hexokinase, a confirmatory finding for the modeling assumptions of $^{18}$F-FDG kinetics, in which $k_3$ is interpreted as a measure of hexokinase activity.[15] This gene was one of the shared genes between $k_3$ and Kis, and was present in both pathways correlated to Kis.

Moreover, the other genes that established the significance of the pathways for Kis were correlated to Fes, in line with the composition of the net uptake rate ($Ki=k_3$ Fe).

### Limitations

Length-scale analysis is not limited by precise anatomical boundaries. Consequently, anatomical interpretations were derived from known sizes of structures and not the structures themselves. Tidal strain calculated from breath-hold images may not reflect fast dynamics and regional differences in inflation time constants. Aeration data derived from tidal breathing images, which represent an average of different phases of the breath cycle, and could be partially influenced by time constants. The advantage of having an *in vivo* measurement brings the confounding factor of blood contributing to regional density. Correlations between regional $^{18}$F-FDG kinetic parameters and gene expression were performed without corrections for multiple comparisons increasing the probability of false positives. However, for pathway identification, we imposed the additional restriction of having two or more genes that represented a proportion of the correlated genes significantly larger than the proportion of the complete pathway in sheep genome (EASE<0.1). These restrictions increased the power of the analysis.

## Conclusion:

In normal and initially injured lungs mechanically ventilated with low tidal volume, small length-scales contribute most to spatial heterogeneity of aeration and tidal strain. Yet, their spatial distributions are not equivalent. Strain heterogeneity length-scales are characterized by larger sizes, comparable to the secondary pulmonary lobule, than those composing aeration heterogeneity. Contributions of length-scales >10 mm to aeration and strain heterogeneity increase with lung injury and with supine position. These changes could represent injurious mechanical conditions, and assessing aeration and strain with large ROIs may delay identification of such conditions. During the initial 20h of injury, molecular image-guided gene expression analysis reveals a topographically heterogeneous activation of the immune system and fluid regulation in lung parenchyma.

## Acknowledgments

This work was supported by the National Institutes of Health [R01 grant HL121228]. The authors thank Steve Weise and Kira Grogg, Department of Radiology, Massachusetts General Hospital, Boston, Massachusetts, for the expert technical support with computed tomography and positron emission tomographic imaging.

## Appendix

**Table A.1 -**

Complementary significant pathways amongst the genes that were correlated to the tissue-specific 18F-FDG volume of distribution and the tissue fraction. A pathway was considered significant if at least two of its' genes were on the analyzed list and had a EASE<0.l.

| Parameter | Group | Pathways |
|---|---|---|
| **Tissue specific volume of distribution (Fes)** | **Diseases** | Alzheimer's disease, Huntington's disease, Salmonella infection, Pertussis, Legionellosis, Leishmaniasis, Chagas' disease, African |

| Parameter | Group | Pathways |
|---|---|---|
| | | trypanosomiasis, Malaria, Toxoplasmosis, Amoebiasis, Tuberculosis, Hepatitis B, Measles, Influenza A, HTLV-1 infection, Herpes simplex infection, Proteoglycans cancer, Asthma, Inflammatory bowel disease, Rheumatoid arthritis, Allograft rejection, Graft-versus-host disease, Type I diabetes mellitus, Non-alcoholic fatty liver disease |
| | **Other systems** | Prolactin signaling, Osteoclast differentiation |
| **Tissue fraction (Ftiss)** | **Diseases** | Salmonella infection, Pertussis, Leishmaniasis, Chagas' disease, Influenza A, Pathways in cancer |
| | **Nervous system** | Long-term depression |

## Simulated Example of Length-Scales

As a visual support of the concept of length-scale and the low-pass filtering analysis consider Figure A.1 where the same global heterogeneity is represented with different black and white check board patterns. The different sizes for the squares (5, 15 and 30 units) are presented with the respective relative contributions of length-scales from 5 to 35 mm.

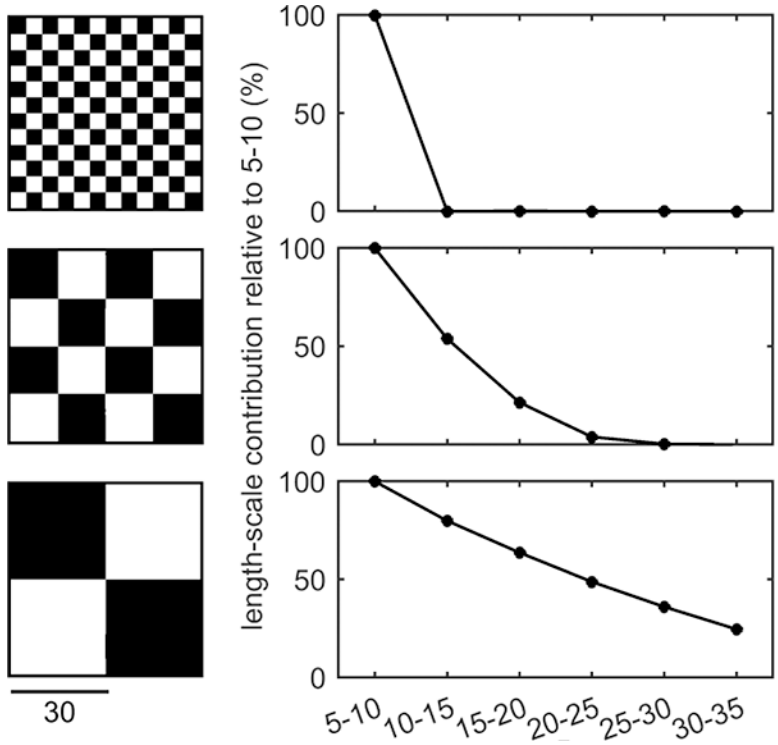


**Figure A. 1 -**

Example of length-scale analysis with the multiple low-pass filter technique applied to check board patterns. All check boards have the same dimensions and total heterogeneity with size of white and black squares increasing from top to bottom.

## References

1. Wellman TJ, Winkler T, Costa EL, et al. Effect of local tidal lung strain on inflammation in normal and lipopolysaccharide-exposed sheep*. Crit Care Med 2014; 42:e491–500. [PubMed: 24758890]
2. Grasso S, Terragni P, Mascia L, et al. Airway pressure-time curve profile (stress index) detects tidal recruitment/hyperinflation in experimental acute lung injury. Crit Care Med 2004; 32:1018–1027. [PubMed: 15071395]
3. Rodarte JR, Chaniotakis M, Wilson TA. Variability of parenchymal expansion measured by computed tomography. J Appl Physiol (1985) 1989; 67:226–231. [PubMed: 2759946]
4. Suki B, Stamenović D, Hubmayr R. Lung Parenchymal Mechanics In: Comprehensive Physiology. John Wiley & Sons, Inc, 2011.
5. Mead J, Takishima T, Leith D. Stress distribution in lungs: a model of pulmonary elasticity. J Appl Physiol 1970; 28:596–608. [PubMed: 5442255]
6. Protti A, Cressoni M, Santini A, et al. Lung stress and strain during mechanical ventilation: any safe threshold? Am J Respir Crit Care Med 2011; 183:1354–1362. [PubMed: 21297069]
7. Gonzalez-Lopez A, Garcia-Prieto E, Batalla-Solis E, et al. Lung strain and biological response in mechanically ventilated patients. Intensive Care Med 2012; 38:240–247. [PubMed: 22109653]
8. Paula LF, Wellman TJ, Winkler T, et al. Regional Tidal Lung Strain in Mechanically Ventilated Normal Lungs. J Appl Physiol (1985) 2016:jap.00861.2015.
9. Gattinoni L, Carlesso E, Cadringher P, Valenza F, Vagginelli F, Chiumello D. Physical and biological triggers of ventilator-induced lung injury and its prevention. Eur Respir J Suppl 2003; 47:15s–25s. [PubMed: 14621113]

10. Wellman TJ, de Prost N, Tucci M, et al. Lung Metabolic Activation as an Early Biomarker of Acute Respiratory Distress Syndrome and Local Gene Expression Heterogeneity. Anesthesiology 2016; 125:992–1004. [PubMed: 27611185]
11. Schroeder T, Vidal Melo MF, Musch G, Harris RS, Venegas JG, Winkler T. Image- derived input function for assessment of 18F-FDG uptake by the inflamed lung. J Nucl Med 2007; 48:1889–1896. [PubMed: 17942803]
12. de Prost N, Feng Y, Wellman T, et al. 18F-FDG kinetics parameters depend on the mechanism of injury in early experimental acute respiratory distress syndrome. J Nucl Med 2014; 55:1871–1877. [PubMed: 25286924]
13. Okazumi S, Isono K, Enomoto K, et al. Evaluation of liver tumors using fluorine-18-fluorodeoxyglucose PET: characterization of tumor and assessment of effect of treatment. J Nucl Med 1992; 2; 33:333–339.
14. Dimitrakopoulou-Strauss A, Strauss LG, Burger C, et al. Prognostic aspects of 18F- FDG PET kinetics in patients with metastatic colorectal carcinoma receiving FOLFOX chemotherapy. J Nucl Med 2004; 45:1480–1487. [PubMed: 15347714]
15. Schroeder T, Vidal Melo MF, Musch G, Harris RS, Venegas JG, Winkler T. Modeling Pulmonary Kinetics of 2-Deoxy-2-[(18)F]fluoro-d-glucose During Acute Lung Injury. Acad Radiol 2008; 15:763–775. [PubMed: 18486012]
16. Acute Respiratory Distress Syndrome Network. Ventilation with lower tidal volumes as compared with traditional tidal volumes for acute lung injury and the acute respiratory distress syndrome. The Acute Respiratory Distress Syndrome Network. N Engl J Med 2000; 342:1301–1308. [PubMed: 10793162]
17. Vidal Melo MF, Layfield D, Harris RS, et al. Quantification of regional ventilation- perfusion ratios with PET. J Nucl Med 2003; 44:1982–19 [PubMed: 14660725]
18. Harris RS, Willey-Courand DB, Head CA, Galletti GG, Call DM, Venegas JG. Regional VA, Q, and VA/Q during PLV: effects of nitroprusside and inhaled nitric oxide. J Appl Physiol 2002; 92:297–312. [PubMed: 11744673]
19. Rota Kops E, Herzog H, Schmid A, Holte S, Feinendegen LE. Performance characteristics of an eight-ring whole body PET scanner. J Comput Assist Tomogr 1990; 14:437–445. [PubMed: 2186064]
20. Wellman TJ, Winkler T, Vidal Melo MF. Modeling of Tracer Transport Delays for Improved Quantification of Regional Pulmonary F-FDG Kinetics, Vascular Transit Times, and Perfusion. Ann Biomed Eng 2015; 43:2722–2734. [PubMed: 25940652]
21. Grogg KS, Toole T, Ouyang J, et al. National Electrical Manufacturers Association and Clinical Evaluation of a Novel Brain PET/CT Scanner. J Nucl Med 2016; 57:646–652. [PubMed: 26697961]
22. Tustison NJ, Avants BB. Explicit B-spline regularization in diffeomorphic image registration. Front Neuroinform 2013; 7:39. [PubMed: 24409140]
23. Reinhardt JM, Ding K, Cao K, Christensen GE, Hoffman EA, Bodas SV. Registration-based estimates of local lung tissue expansion compared to xenon CT measures of specific ventilation. Med Image Anal 2008; 12:752–763. [PubMed: 18501665]
24. Kaczka DW, Cao K, Christensen GE, Bates JHT, Simon BA. Analysis of regional mechanics in canine lung injury using forced oscillations and 3D image registration. Annals of Biomedical Engineering 2011; 39:1112–1124. [PubMed: 21132371]
25. Choi S, Hoffman EA, Wenzel SE, et al. Registration-based assessment of regional lung function via volumetric CT images of normal subjects vs. severe asthmatics. J Appl Physiol (1985) 2013; 115:730–742. [PubMed: 23743399]
26. Du K, Bayouth JE, Cao K, Christensen GE, Ding K, Reinhardt JM. Reproducibility of registration-based measures of lung tissue expansion. Med Phys 2012; 39:1595–1608. [PubMed: 22380392]
27. Murphy K, van Ginneken B, Pluim JP, Klein S, Staring M. Semi-automatic reference standard construction for quantitative evaluation of lung CT registration. Med Image Comput Comput Assist Interv 2008; 11:1006–1013. [PubMed: 18982703]
28. Ikeda M, Makino R, Imai K, Matsumoto M, Hitomi R. A method for estimating noise variance of CT image. Computerized Medical Imaging and Graphics 2010; 34:642–650. [PubMed: 20797837]

29. Christianson O, Winslow J, Frush DP, Samei E. Automated Technique to Measure Noise in Clinical CT Examinations. Am J Roentgenol 2015; 205:W93–W99. [PubMed: 26102424]
30. Vidal Melo MF, Winkler T, Harris RS, Musch G, Greene RE, Venegas JG. Spatial heterogeneity of lung perfusion assessed with (13)N PET as a vascular biomarker in chronic obstructive pulmonary disease. J Nucl Med 2010; 51:57–65. [PubMed: 20008987]
31. Borges JB, Okamoto VN, Matos GF, et al. Reversibility of lung collapse and hypoxemia in early acute respiratory distress syndrome. Am J Respir Crit Care Med 2006; 174:268–278. [PubMed: 16690982]
32. Wellman TJ, Winkler T, Costa EL, et al. Effect of regional lung inflation on ventilation heterogeneity at different length scales during mechanical ventilation of normal sheep lungs. J Appl Physiol 2012; 113:947–957. [PubMed: 22678958]
33. Venegas JG, Galletti GG. Low-pass filtering, a new method of fractal analysis: application to PET images of pulmonary blood flow. J Appl Physiol 2000; 88:1365–1373. [PubMed: 10749831]
34. Huang da W, Sherman BT, Lempicki RA. Systematic and integrative analysis of large gene lists using DAVID bioinformatics resources. Nat Protoc 2009; 4:44–57. [PubMed: 19131956]
35. Sapoval B, Filoche M, Weibel ER. Smaller is better—but not too small: A physical scale for the design of the mammalian pulmonary acinus. Proceedings of the National Academy of Sciences 2002; 99:10411–10416.
36. Webb WR. Thin-Section CT of the Secondary Pulmonary Lobule: Anatomy and the Image—The 2004 Fleischner Lecture. Radiology 2006; 239:322–338. [PubMed: 16543587]
37. Mertens M, Tabuchi A, Meissner S, et al. Alveolar dynamics in acute lung injury: heterogeneous distension rather than cyclic opening and collapse. Crit Care Med 2009; 37:2604–2611. [PubMed: 19623041]
38. Perlman CE, Bhattacharya J. Alveolar expansion imaged by optical sectioning microscopy. J Appl Physiol 2007; 103:1037–1044. [PubMed: 17585045]
39. Bayat S, Porra L, Albu G, et al. Effect of positive end-expiratory pressure on regional ventilation distribution during mechanical ventilation after surfactant depletion. Anesthesiology 2013; 119:89–100. [PubMed: 23559029]
40. Cereda M, Emami K, Xin Y, et al. Imaging the interaction of atelectasis and overdistension in surfactant-depleted lungs. Crit Care Med 2013; 41:527–535. [PubMed: 23263577]
41. Olson LE, Rodarte JR. Regional differences in expansion in excised dog lung lobes. J Appl Physiol 1984; 57:1710–1714. [PubMed: 6511545]
42. Glenny RW. Emergence of matched airway and vascular trees from fractal rules. J Appl Physiol 2011; 110:1119. [PubMed: 21164156]
43. Dolinay T, Kaminski N, Felgendreher M, et al. Gene expression profiling of target genes in ventilator-induced lung injury. Physiol Genomics 2006; 26:68–75. [PubMed: 16569776]
44. Copland IB, Kavanagh BP, Engelberts D, McKerlie C, Belik J, Post M. Early changes in lung gene expression due to high tidal volume. Am J Respir Crit Care Med 2003; 168:1051–1059. [PubMed: 12816737]
45. Spooner CE, Markowitz NP, Saravolatz LD. The role of tumor necrosis factor in sepsis. Clinical Immunology and Immunopathology 1992; 62:S11–S17. [PubMed: 1370262]
46. Liu SF, Malik AB. NF-kappaB activation as a pathological mechanism of septic shock and inflammation. Am J Physiol Lung Cell Mol Physiol 2006; 290:L622. [PubMed: 16531564]
47. Brubaker SW, Bonham KS, Zanoni I, Kagan JC. Innate Immune Pattern Recognition: A Cell Biological Perspective. Annu Rev Immunol 2015; 33:257–290 [PubMed: 25581309]
48. Cereda M, Xin Y, Hamedani H, et al. Tidal changes on CT and progression of ARDS. Thorax 2017.
49. Olivera W, Ciccolella D, Barquin N, et al. Aldosterone Regulates Na,K-ATPase and Increases Lung Edema Clearance in Rats. Am J Respir Crit Care Med 2000; 161:567–573. [PubMed: 10673201]

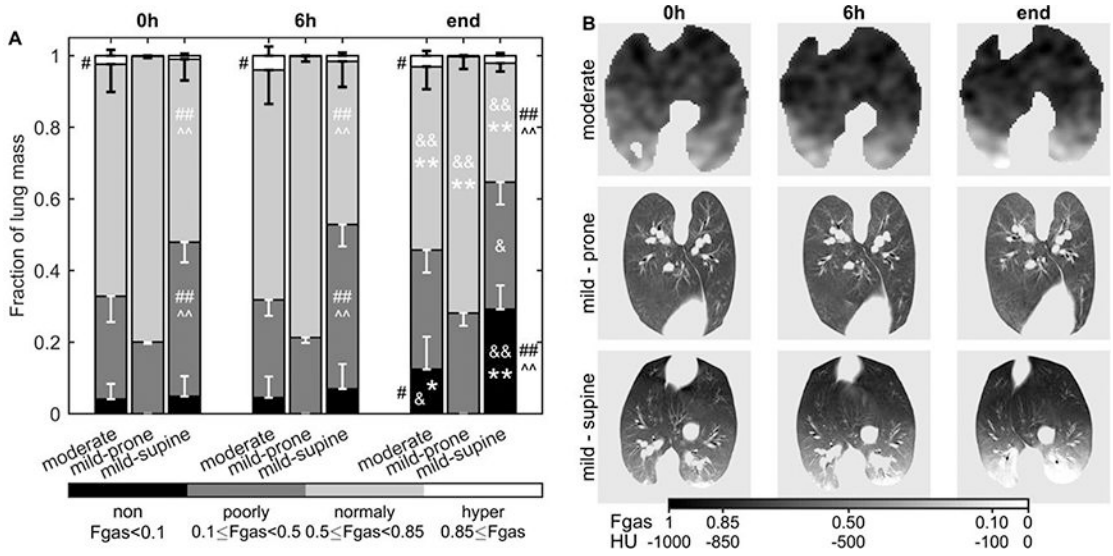


**Figure 1-**

Lung aeration in sheep mechanically ventilated with low tidal volume and low to moderate positive and-expiratory pressure for 20–24h. After the first measurement, intravenous infusion of LPS was started to generate moderate (10 ng/kg/min) or mild (2.5 ng/kg/min) systemic endotoxemia. Aeration was quantified as the gas fraction (Fgas) in each voxel of transmission (moderate group) and computed tomography (mild groups) scans during tidal ventilation. (A) Non- (black), poorly- (dark grey), normally- (light grey) and hyper-aerated (white) compartments are expressed as a fraction of total lung mass. Irrespective of the endotoxin dose, non-aerated regions increased after 20h in supine, but not in prone animals. For supine sheep, the spatial distribution of aeration followed a gravitational gradient decreasing toward dorsal regions (B). Aeration level at 24h * vs 0h and & vs 6h for the same group; ^ vs moderate and # vs mild-prone for the same aeration compartment; one symbol $p<0.05$, two symbols $p<0.001$.

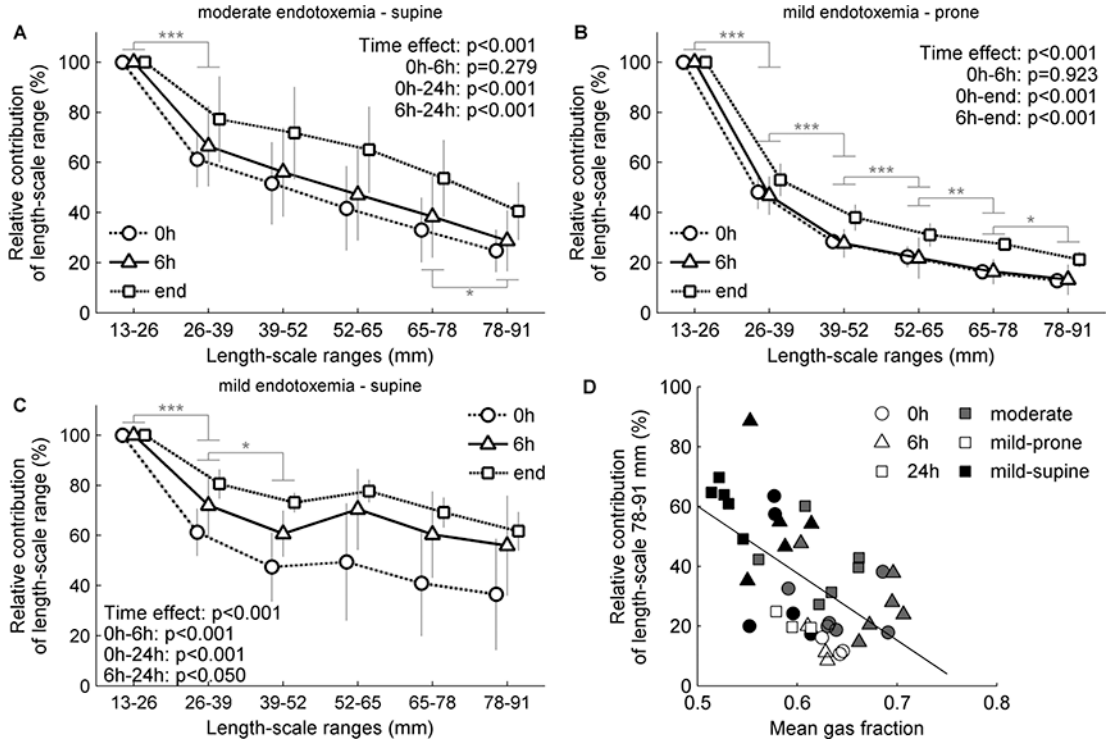


**Figure 2-**

Contribution of length-scale ranges to lung aeration heterogeneity. Sheep with moderate (A, 10 ng/kg/min LPS) or mild (B-C, 2.5 ng/kg/min LPS) endotoxemia were mechanically ventilated using low tidal volume and low to moderate positive end- expiratory pressure. The contribution of a length-scale range was assessed by the difference between the variances normalized by the square mean in mean lung volume images filtered for effective resolutions from 13 to 91 mm. Values were expressed relative to the smallest length-scale (13–26 mm). In both endotoxemia levels and body positions (supine, A and C, prone, B), the largest contribution to heterogeneity was in the length-scale 13–26 mm, with an increase in the contribution of larger length-scales along time. Contribution of larger length-scales decreased with the mean gas fraction (D).* $p<0.05$, ** $p<0.01$ and *** $p<0.001$ for differences between consecutive length-scales.

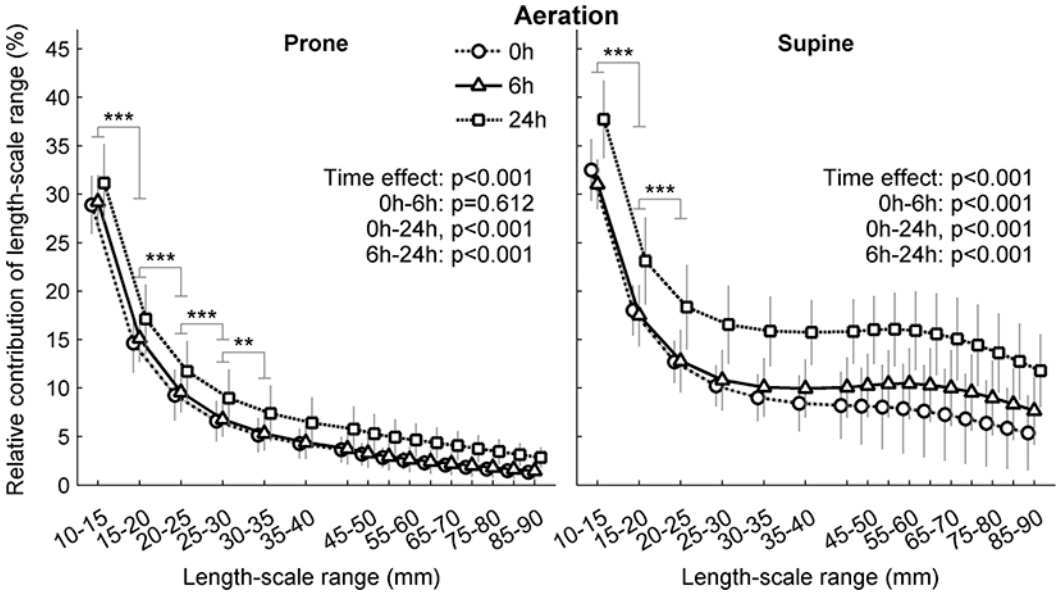


**Figure 3-**

Contribution of length-scale ranges to lung aeration heterogeneity for mildly endotoxemic sheep in prone (left) and supine (rigth) positions. Animals were mechanically ventilated with low tidal volume and low positive end-expiratory pressure for 24h. The contribution of a length-scale range was assessed by the difference between the variances normalized by the square mean in images filtered for effective resolutions from 5 to 90 mm. Values were expressed relative to the smallest length-scale (5–10 mm). While both body positions displayed their largest contribution to heterogeneity in length-scale 5–10 mm, supine animals (right) showed substantially higher contribution of larger length-scales than prone (left). ** p<0.01 and *** p<0.001 for differences between consecutive length-scales.

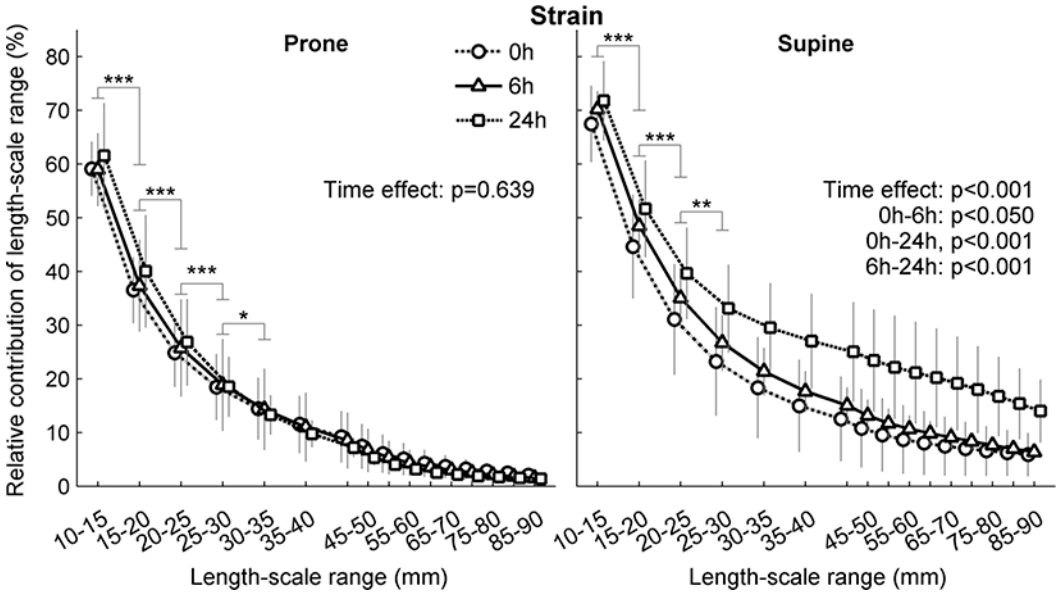


**Figure 4-**

Contribution of length-scale ranges to lung tidal strain heterogeneity for mildly endotoxemic sheep in prone (left) or supine (right) positions. Animals were mechanically ventilated with low tidal volume and low positive end-expiratory pressure for 24h. The contribution of a length-scale was assessed by the difference between the variances normalized by the square mean in images filtered for effective resolutions from 5 to 90 mm. Values were expressed relative to the smallest length-scale (5–10 mm). Supine had higher relative contributions of all length-scales and showed significant change at 6 and 24h. Prone had no difference between time points. * $p<0.05$, ** $p<0.01$ and ** $p<0.001$ for differences between consecutive length-scales. Strain was calculated with an initial B-spline knot distance of 26 mm.

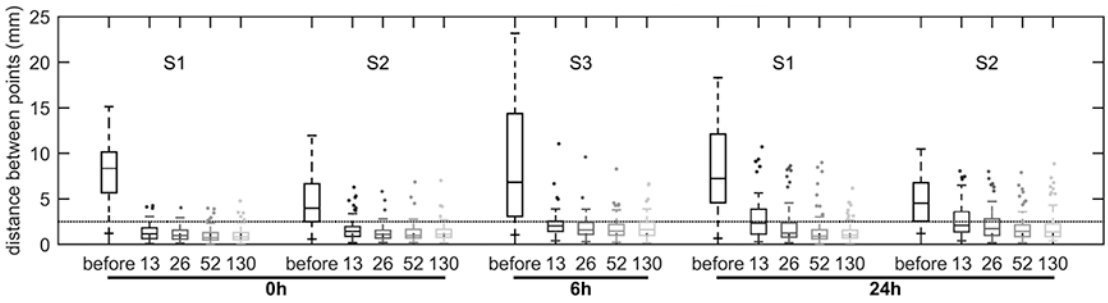


**Figure 5-**

Distance between landmark points matched in the expiratory and inspiratory images before and after image registration using different distances for the knots of the B-spline regularization (13, 26, 52 and 130 mm). Landmark distance was used as a measure of overall image registration accuracy. Data correspond to two randomly selected supine sheep (S1 and S2) at the beginning (0h) and end of the experiment (24h). These time points were chosen because they represent the extremes in aeration and atelectasis. A measurement at 6h of a third sheep (S3) was added because it represented the study with the largest gas volume difference between inspiratory and expiratory images. An average of 95.8 points [range 74–122] were used for each animal-time point combination. Landmarks were semi-automatically matched in each pair of images by one observer. Dotted line represents the largest dimension of image voxels (2.5 mm). The B-spline knots' distance corresponds to the first stage of registration.

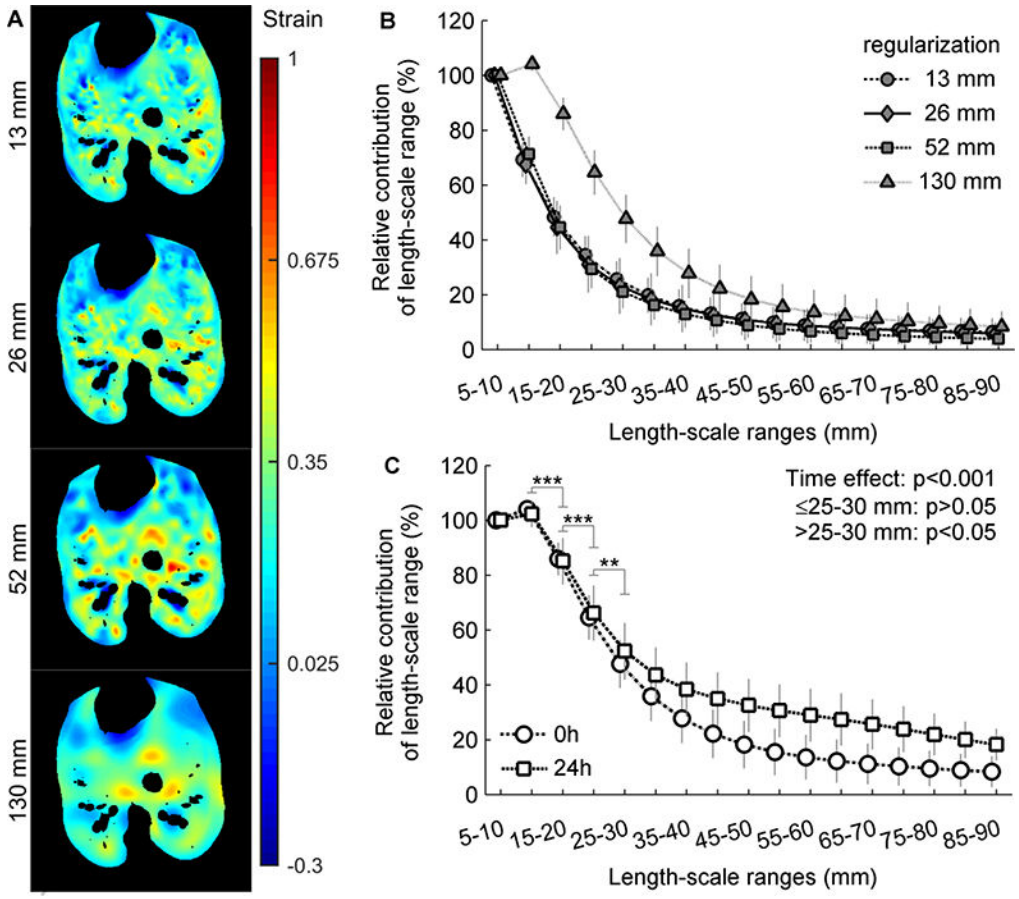


**Figure 6-**

Contribution of length-scale ranges to lung tidal strain heterogeneity. Mildly endotoxemic (2.5 ng/kg/min LPS) supine sheep were mechanically ventilated using low tidal volume and low positive end-expiratory pressure. Voxel level strain was estimated using different distances between the knots of the B-spline regularization (13, 26, 52 and 130 mm in the first step). The contribution of a length-scale was assessed by the difference between the variances normalized by the squared mean in images filtered for effective resolutions from 5 to 35 mm. Values are normalized to the 5–10 mm. Only the baseline data was analyzed, as it was the time point with best agreement in landmarks distance between the four regularization factors. (A) Examples of the spatial distribution of strain estimated with each B-spline knots' distance. Note the increase in size of the regions with similar colors from the upper (13 mm) to the lower (130 mm) images. (B) There was no qualitative difference in contributions of length-scales between 13, 26 and 52 mm. (C) Contribution of length-scale ranges at 0h and 24h for the largest knots' distance showing a significant increase in contribution of length-scales larger than 30 mm after 24h. ** p<0.01 and *** p0.001 for differences between consecutive length-scales.

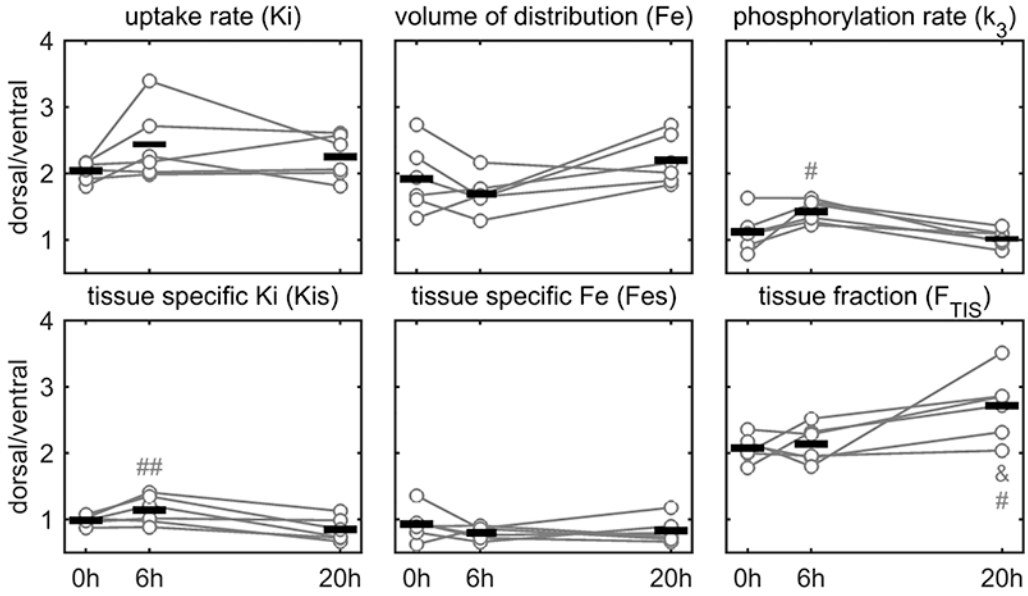


**Figure 7-**

Dorsal/ventral ratio of $^{18}$F-FDG kinetic parameters and tissue fraction in sheep undergoing low tidal volume and low to moderate positive end-expiratory pressure mechanical ventilation, and moderate endotoxemia (10 ng/kg/min LPS). The phosphorylation rate and tissue-specific $^{18}$F-FDG uptake rate at 6h were significantly different from 20h (# $p<0.05$ and ## $p<0.01$) indicating that dorsal and ventral regions started and ended with similar levels, but followed different temporal trajectories. This could indicate different biological process due to differences in aeration, tidal strain, ventilation and perfusion. Tissue fraction increased at dorsal regions at 20h compared to both 6 and 0h (# and & $p<0.05$).

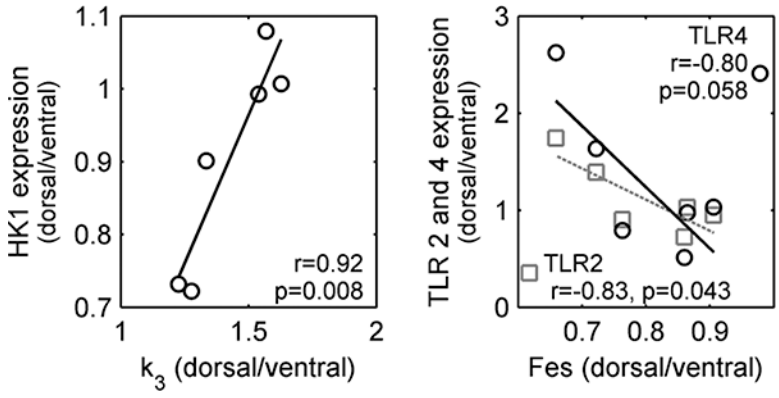


**Figure 8-**

Correlations between dorsal to ventral ratios of selected genes expression and $^{18}$F-FDG kinetic parameters. The transport rate from the non-metabolized to the metabolized compartment ($k_3$), which represents the phosphorylation of $^{18}$F-FDG, was correlated with gene expression of hexokinase (HK1). The $^{18}$F-FDG volume of distribution normalized by tissue fraction (Fes) is normally attributed to the number of neutrophils in the analyzed region and was correlated with the expression of toll-like receptors 2 and 4 (TLR2 and TLR4), which are involved in the process of neutrophil migration and bacteria detection.

**Table 1-**

Noise level estimate in the full resolution mean lung volume CT converted to $F_{GAS}$ and the SD of voxels inside the lung mask after removing gravitational the gradient and filtering with 5 mm kernel.

| | | Oh | 6h | 24h | p-values |
|---|---|---|---|---|---|
| **Ikeda *et. al.*** [28] | | 0.021±0.002 | 0.021±0.002 | 0.021±0.003 | Time = 0.376 |
| **Christianson *et. al.*** [29] | | 0.027±0.003 | 0.026±0.003 | 0.025±0.003 | Method <0.001 |
| **SD within lung** | **supine** | 0.094±0.016 | 0.095±0.013 | 0.127±0.019 | - |
| | **prone** | 0.069±0.001 | 0.066±0.005 | 0.078±0.009 | |

**Table 2-**

Significant pathways amongst the genes that were correlated to $^{18}$F-FDG kinetics parameters and tissue fraction. A pathway was considered significant if at least two of its' genes were on the analyzed list and had EASE<0.l.

| Parameter | Group | Specific pathways |
|---|---|---|
| **Tissue-specific uptake rate (Kis)** | **Metabolism** | Fructose and mannose metabolism, Biosynthesis of antibiotics |
| **Tissue specific volume of distribution (Fes)** | **Environmental information processing** | PI3K-Akt signaling, Calcium signaling, NF-kappa B signaling, Jak-STAT signaling, TNF signaling, Cytokine-cytokine receptor interaction |
| | **Immune system** | Toll-like receptor signaling, T cell receptor signaling, Natural killer cell mediated cytotoxicity, Antigen processing and presentation |
| **Phosphorylation rate ($k_3$)** | **Excretory system** | Aldosterone-regulated sodium reabsorption |
| **Tissue fraction ($F_{TIS}$)** | **Environmental information processing** | Jak-STAT signaling, Neuroactive ligand-receptor interaction |
| | **Immune system** | Toll-like receptor signaling, T cell receptor signaling, RIG-I-like receptor signaling, Hematopoietic cell lineage |